This is the Pre-Published Version.

The following publication Kim, Eunyoung; Chan, Kit-Ying; Yang, Jie; Venkatesan, Harun; Adegun, Miracle Hope; Zhang, Heng; Lee, Jeng-Hun; Shen, Xi; Kim, Jang-Kyo(2023). Engineering anisotropic structures of thermally insulating aerogels with high solar reflectance for energy-efficient cooling applications. Journal of Materials Chemistry A, 11(13), 7105-7114 is available at https://doi.org/10.1039/D2TA09983G.

Engineering anisotropic structures of thermally insulating aerogels with high solar reflectance for energy-efficient cooling applications

Eunyoung Kim,[1]† Kit-Ying Chan,[2]† Jie Yang,[1] Harun Venkatesan,[1] Miracle Hope Adegun,[1] Heng Zhang,[1] Jeng-Hun Lee,[1] Xi Shen,[2,3]* Jang-Kyo Kim[1,4]*

[1] Department of Mechanical and Aerospace Engineering, The Hong Kong University of Science and Technology, Clearwater Bay, Kowloon, Hong Kong

[2] Department of Aeronautical and Aviation Engineering, The Hong Kong Polytechnic University, Hung Hom, Kowloon, Hong Kong

[3] The Research Institute for Sports Science and Technology, The Hong Kong Polytechnic University, Hung Hom, Kowloon, Hong Kong

[4] School of Mechanical and Manufacturing Engineering, The University of New South Wales, Sydney, NSW 2052, Australia

†Eunyoung Kim and Kit-Ying Chan share equal first authorship

*Corresponding authors: Xi Shen (xi.shen@polyu.edu.hk); Jang-Kyo Kim (mejkkim@ust.hk)

Abstract

Aerogel materials with anisotropic nature have attracted increasing interest because of fascinating, potential applications arising from their novel functional capabilities. However, the strategy to achieve highly anisotropic structure of aerogel materials for thermal superinsulation has not been fully exploited. In this work, the microstructure and thermal conductivity (k) of waterborne polyurethane (WPU) aerogels are tailored by using different freezing temperatures ranging from -196 to -20 ºC in unidirectional freeze-casting. A more anisotropic porous aerogel is obtained at a lower freezing temperature, yielding highly different k in two orthogonal directions. The anisotropy of WPU aerogels is further intensified with the addition of two-dimensional boron nitride nanosheets (BNNS) possessing anisotropic k values and a high reflectance. Surprisingly, an ultralow density of 20.2 mg/cm^3 is achieved by the composite

aerogel freeze-dried at -196 ºC, much lower than the WPU matrix acting alone, by creating more pores of smaller sizes. The unique thermo-optical properties of BNNS in highly aligned cell walls of the BNNS/WPU composite aerogels endow fast heat dissipation in the alignment direction while largely diminished heat transfer through the thickness direction, achieving an ultralow *k* of 16.2 mW/m K for thermal superinsulation. A new theoretical approach is also proposed to estimate the anisotropic *k* of porous materials, verifying the positive roles played by BNNS in efficient thermal management for directional insulation. In addition, the presence of abundant pores and reflective BNNS is responsible for the excellent solar reflectance (~97%) of the aerogels. The coupling effect of highly anisotropic *k* and high sunlight reflectance offers better thermal management under direct sunlight with up to 6 ºC lower internal temperature than the commercial SiO_2 blanket and expanded polystyrene foam coated with commercial reflective paint in the outdoor test. This work can provide general guidelines in designing and producing highly anisotropic aerogels for more energy efficient cooling applications.

1. Introduction

The energy consumption for thermal regulation (i.e., space cooling and heating), especially in residential buildings, has been continuously increasing.[1-3] To reduce the dependency on electrical cooling, thermally insulating materials, such as expanded polystyrene (EPS) and polyurethane (PU) foams, have been widely used to maintain a comfortable interior environment. To minimize the heat exchange between external and internal environments, advanced thermally insulating materials, such as gas-filled panels and aerogels, have been developed to achieve low thermal conductivities (k).[2, 3] Significant research efforts[4-8] have also been devoted to developing superinsulating, anisotropic aerogels with k lower than that of air (k_{air} = 24 mW/m K). Thanks to the high k in the pore alignment direction (k_{align}) for effective heat dissipation, the heat transfer in the through-thickness direction (k_{trans}) of anisotropic aerogels can be significantly reduced, exhibiting a better thermal management capability than their isotropic counterparts.[9] Anisotropic thermal management materials are commonly characterized by the anisotropic factor (R), which is the ratio of k_{align}-to-k_{trans}.[10] Although experimental studies and theoretical calculations have been carried out to highlight the contribution of anisotropic heat transfer behaviors of aerogel materials for building applications,[9] the diminished k_{trans} is normally accompanied by the concurrently reduction in the k_{align} due to the similar mechanisms in heat transfer in the two directions. No clear strategy has thus far been proposed in controlling the anisotropic factor of aerogels. As such, it is very desirable to establish a synergistic mechanism to reduce the k_{trans} without significantly affecting the k_{align} through controlling both the material and processing parameters in the fabrication of highly anisotropic aerogels for more energy-efficient cooling applications.

To achieve a high R of aerogel, one effective strategy is to use building blocks with intrinsically high anisotropic k. Two-dimensional (2D) materials, such as graphene and hexagonal boron nitride (*h*-BN), are typical anisotropic conductors with high intrinsic R of ~ 300 and 87, respectively.[11, 12] They have been extensively used as nanofillers in nanocomposites

and aerogels for thermal management applications.[13, 14] Despite a higher *R* of graphene than *h*-BN, the intrinsic light absorption of graphene and its derivatives leads unwanted solar heat gains, unable to offer superinsulation performance for outdoor daytime applications.[7] By contrast, *h*-BN with a large band gap of 5.765 eV[15] can only absorb light with wavelengths up to ~215 nm. Therefore, *h*-BN and exfoliated BN nanosheets (BNNS) have great potential in minimizing the solar heat gain for thermal insulators.[16] Nonetheless, BNNS/polymer nanocomposites have been mainly explored in personal[17] and electronics[18] cooling applications owing to their high in-plane *k* that can facilitate rapid heat dissipation, while limited efforts have been directed to the potential thermal insulation applications of BNNS aerogels.[19, 20] Moreover, the reported works have not paid much attention to the low out-of-plane *k* of BNNS, meaning that the anisotropic *k* of BNNS has yet to be fully exploited.

In addition to exploiting the intrinsic anisotropic *k* of BNNS, engineering the anisotropic microstructure is also necessary to translate the anisotropic *k* of BNNS to bulk aerogels. Directional freeze-casting is a common approach to fabricate anisotropic aerogel materials because it is environmentally friendly and cheap.[21, 22] More importantly, the microstructure of aerogels can be tailored by varying the freezing parameters such as freeze temperature.[23-25] Previous studies have focused on the effects of freezing temperature on mechanical properties,[26-28] electromagnetic interference shielding,[29, 30] filtration efficiency,[31] optical absorption,[32] microwave absorption,[33] and capacitive performance.[34] Although a few studies have reported the effects of freezing temperature on *k* of anisotropic aerogels, they only concentrated on *k* in one direction, either in the alignment direction[35] or transverse to it.[32] None of them so far reported the relationship between freezing temperature and anisotropic *k* of aerogel materials.

In this work, the anisotropic factor (*R*) of waterborne polyurethane (WPU) aerogels was tailored by controlling the freezing temperature used in the unidirectional freeze-casting process and the addition of BNNS, as shown in Figure 1a. Different freezing temperatures caused

different freezing dynamics (Figure 1b), resulting in distinct microstructures where smaller pore sizes and better aligned pore channels were achieved at a lower freezing temperature after freeze-drying (Figure 1c). The pore size of aerogel was further reduced when BNNS were added in WPU because of the heterogeneous nucleation of ice crystals on the BNNS surface during the freeze-casting process. The better pore alignments at a lower freezing temperature and the anisotropic k of BNNS were exploited to achieve a high R value of 6 and an ultralow k_{trans} of 16.2 mW/m K in the BNNS/WPU composite aerogel freeze-cast at – 196 °C. The k value is 32.5% lower than k_{air}, demonstrating excellent thermal insulation performance. Combined together with the excellent solar reflectance of ~97%, the BNNS/WPU aerogels maintained an up to 6 °C lower internal temperature under direct sunlight than commercial SiO_2 aerogel blanket and EPS foam coated with reflective paint, showing great potential for more energy-efficient cooling in building applications.

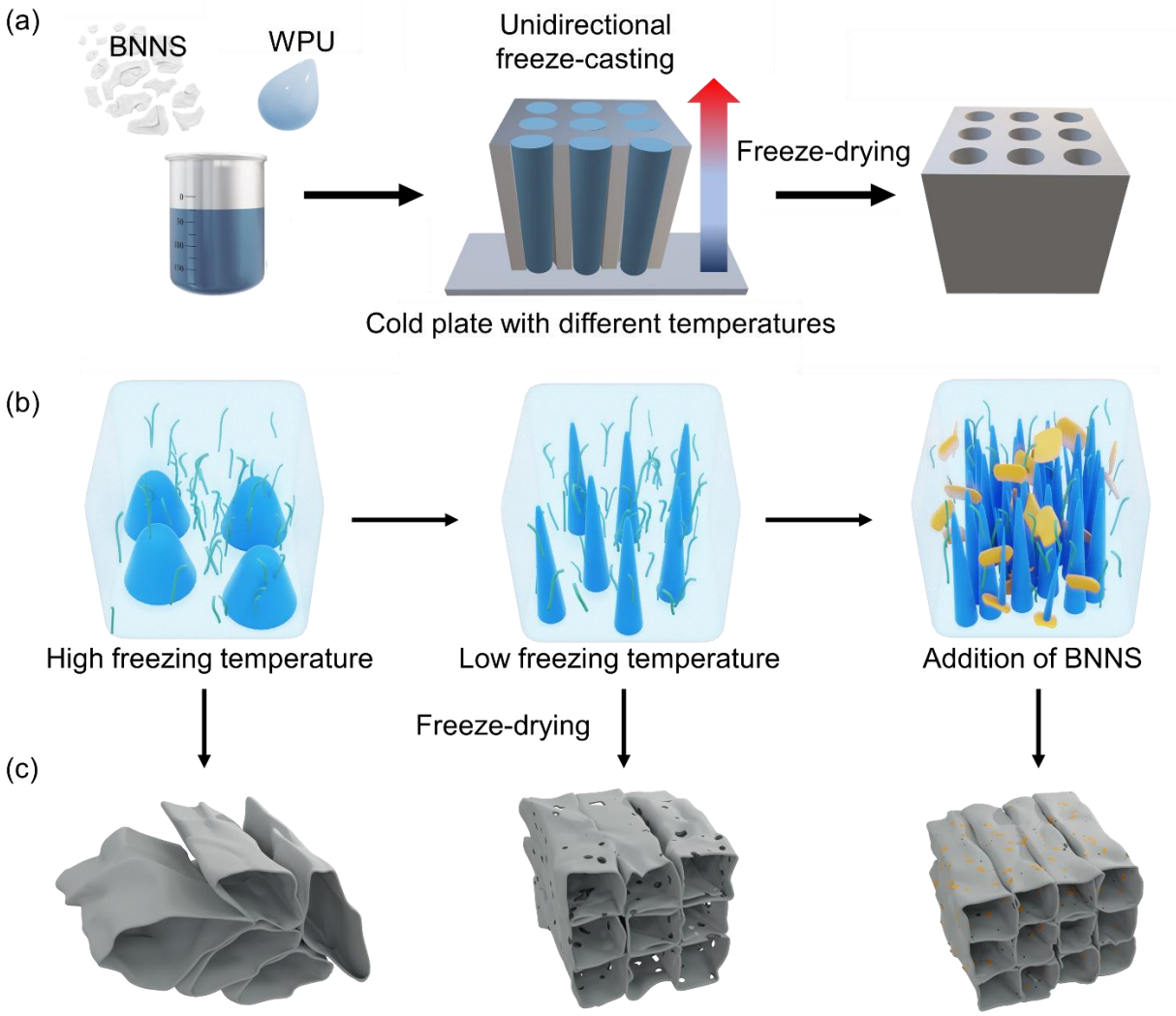

Figure 1. Fabrication process of anisotropic WPU aerogels. (a) Schematic of the set-up and operating principle of unidirectional freeze-casting at different freezing temperatures. Schematics of the effects of freezing temperature and BNNS fillers on (b) the freezing dynamics and (c) the resulting anisotropic microstructures of aerogels.

2. Results and discussion

2.1 Physical properties and microstructures of BNNS/WPU composite aerogels

The morphologies and chemical compositions of exfoliated BNNS from bulk *h*-BN were characterized (Supplementary Figure 1, see details in Supplementary Information). The Fourier-transform infrared (FTIR) spectra of BNNS, WPU aerogel and BNNS/WPU aerogel revealed the successful incorporation of BNNS into the WPU aerogel (Figure 2a). Two

absorption peaks of BNNS at 800 and 1380 cm^{-1} correspond to the B-N bending and stretching, respectively, while WPU presented absorption peaks for the stretching vibration of C-O (1095 and 1238 cm^{-1}), C=O (1705 cm^{-1}), C-H (2853, 2945 cm^{-1}), N-H bonds (1531 and 3298 cm^{-1}) from the urethane groups. The BNNS/WPU composite showed absorption peaks of both BNNS and WPU, confirming the incorporation of BNNS in WPU.[36, 37] The X-ray photoelectron spectroscopy (XPS) spectra of WPU and BNNS/WPU aerogels (Supplementary Figure 1e-f) indicate the presence of hydroxyl groups on BNNS, which could form hydrogen bonds with the ether or carboxyl groups in the WPU chains to promote the interfacial interaction between the two.[38] In addition to hydrogen bonds, π-π stacking was also likely to form between the aromatic rings in WPU and the hexagonal B-N rings in BNNS,[39] further enhancing their interfacial interaction. Both the WPU and BNNS/WPU aerogels exhibited ultralow densities (Figure 2b) and high porosities (Figure 2c). The pristine WPU aerogels with a low WPU concentration of 1.4 wt% had densities in a range of 26 – 37 mg/cm^3, which decreased with decreasing the freezing temperature, whereas their high porosities of ≥ 96% remained little variation with freezing temperature. Under different freezing dynamics induced by different freezing temperatures, distinct microstructures of WPU aerogels were realized, as shown in Figure 2d-f. At a high freezing temperature (i.e., − 20 ˚C), the slow ice solidification rate (Figure 1b) generated large pore sizes, leading to the collapse of pores that appeared like scattered flakes after freeze-drying (Figure 1c), and unable to form an intact shape, as shown in Figure 2d and 2g. The collapsing pores can explain the high density of 36.7 mg/cm^3 of WPU aerogels fabricated using a high freezing temperature of − 20 ˚C (Figure 2b). By lowering the freeze temperature to − 50 ˚C, the pore sizes were decreased while the pore alignments were improved (Figure 2e and 2h). At a much lower freezing temperature (i.e., − 196 °C), the significant supercooling promoted the nucleation rate and suppressed the ice growth rate while the large temperature gradient facilitated the highly directional growth (Figure 1b),[40] allowing the

formation of smaller ice crystals and thus smaller pores with more rigid, highly-aligned cell walls, as shown in Figure 2f and 2i.

To further minimize the shrinkage and improve the pore alignment of WPU aerogels, 10 wt% BNNS was added in the 1.4 wt% WPU solution. Surprisingly, the incorporation of BNNS decreased the densities of WPU aerogels regardless of the freezing temperature, despite their higher density (2.25 g/cm^3) than that of WPU (1.02 g/cm^3). An ultralow density of 20.2 mg/cm^3 was achieved by the composite aerogel freeze-dried at − 196 ºC. This value is 21% lower than its WPU counterpart obtained at the same freezing temperature, manifested by a higher porosity and a lower shrinkage. The strong and stiff BNNS fillers effectively reinforced the WPU cell walls, giving rise to less volume shrinkage during the freeze-drying process which in turn resulted in lower densities of composite aerogels than their WPU counterparts.[8] This ameliorating functional feature came together with the potentially enhanced structural robustness of cell walls arising from the better aligned cell walls and smaller pore sizes with BNNS (Figure 2j and 2k) than the WPU aerogel acting alone (Figure 2f and 2i). The heterogeneous nucleation of ice crystals on BNNS surfaces leading to the enhanced nucleation rate at the same temperature[40] (Figure 1b) was responsible for the smaller pore sizes in the BNNS/WPU composites aerogels.

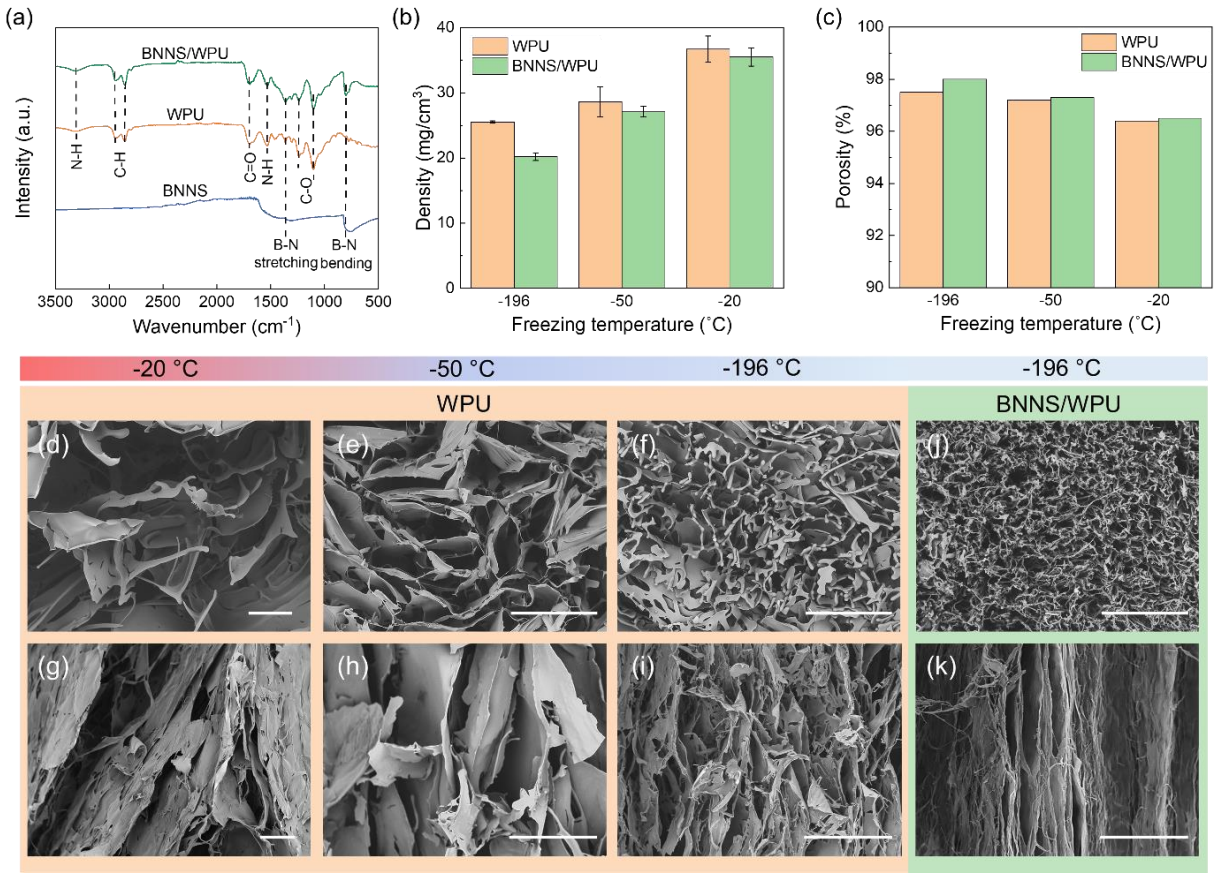

Figure 2. Physical properties and microstructures of WPU aerogels. (a) FTIR patterns of BNNS, WPU aerogel and BNNS/WPU aerogel. (b) Density and (c) porosity of WPU and BNNS/WPU aerogels obtained at different freezing temperatures. Scanning electron microscope (SEM) images showing the (d-f) cross-section and (g-i) pore alignment of pristine WPU aerogels prepared at different freezing temperatures. SEM images showing the (j) cross-section and (k) pore alignment of BNNS/WPU composite aerogel freeze-dried at -196 ˚C. Scale bars: 500 μm.

2.2 Anisotropic thermal insulation properties of BNNS/WPU composite aerogels

Anisotropic *k* could provide an effective thermal insulation by dissipating the heat rapidly along the alignment direction while discouraging heat transfer in the transverse direction. To optimize the anisotropic thermal insulation properties, the effect of freezing temperature on anisotropic *k* of WPU and BNNS/WPU composite aerogels were investigated, as shown in

Figure 3a and 3b, respectively. In general, WPU aerogels with only 1.4 wt% solid content showed superior thermal insulation due to the high porosity arising from the low solid conduction. The k_{align} of both WPU and BNNS/WPU aerogels increased with decreasing the freezing temperature, whereas their k_{trans} values showed an opposite trend. It is also shown that the anisotropic factor ($R = k_{align}/k_{trans}$) increased with decreasing the freezing temperature, proving that a highly anisotropic structure was achieved at a lower freezing temperature. During the freeze-drying process, the shrinkage becomes significant for the aerogels fabricated with high freezing temperature due to the formation of large pores that led to a higher possibility of pore collapses (Figure 1c and Figure 2g). This resulted in a poor pore alignment and eventually the connection of the axial cell walls, which allowed the heat conduction not only through the alignment direction but also in the transverse direction, as shown in Figure 3c. By contrast, the pore alignments were improved with a lower freezing temperature, effectively inhibiting the heat transfer through thickness direction (Figure 3c).

The addition of BNNS further enhanced k_{align} while decreasing k_{trans} for the composite aerogels freeze-dried at -196 ˚C and -50 ˚C, yet there was no significant change in k of the aerogel freeze-dried at -20 ˚C (Figure 3b) due to its collapsed pores (Figure 3c). As such, the highly aligned structure of BNNS/WPU aerogel produced by the lowest freezing temperature of -196 ˚C ameliorated the anisotropic k of BNNS, achieving an ultralow k_{trans} of 16.2 mW/m K and a high R of ~6. Its thermal superinsulation performance was confirmed by the thermal response of the top surface when the bottom was heated using a hot plate at ~85 °C, as shown in Supplementary Figure 2. The top-surface temperature of the composite aerogel rose to a steady-state temperature of 31 °C, which was 54 °C lower than the surface of hot plate, while the top surface of commercial EPS foam (k = 30.5 mW/m K) was 5 °C hotter than the aerogel under the same condition.

Interestingly, BNNS, commonly known as a highly thermally conductive material,[40] did not only improve the k_{align} for heat dissipation along the alignment direction, but it also

simultaneously enhanced the thermal insulation in the transverse direction of the BNNS/WPU aerogel freeze-dried at -196 ˚C. To understand the effect of BNNS on anisotropic *k* of aerogels, theoretical models were explored by accounting for the anisotropic thermal transport in the aerogel. Previously, the overall *k* of porous materials were estimated by the sum of four components, namely gas conduction (k_{cond}^{g}), solid conduction (k_{cond}^{s}), convection (k_{conv}) and radiation (k_{rad}), according to Eq. (1)-(3).[4, 7, 41, 42] The effects of convection and radiation can be neglected because the pore size is below the onset size of natural convection, which is 1 mm,[43, 44] and the relatively low application temperature,[43] respectively. Therefore, the heat transfer in the aerogel material is dominated by the gas and solid conduction:

$$k = k_{cond}^{g} + k_{cond}^{s} + k_{conv} + k_{rad} \approx k_{cond}^{g} + k_{cond}^{s} \quad (1)$$

$$k_{cond}^{g} = \frac{k_0^{g}\varphi}{1+2\beta K_n} \quad (2)$$

$$k_{cond}^{s} = \frac{k_0^{s}}{1+k_0^{s}\frac{R_{BD}}{d}} \quad (3)$$

where k_0^{g} is the *k* of air (24 mW/m K), φ is the porosity of aerogel, β is a constant with ~2 for air, K_n is Knudsen number which is defined by the ratio of the mean free path of a gas molecule (~70 nm) to the average pore size, k_0^{s} is weighted average solid conduction of the individual components, R_{BD} is the Kapitza interfacial thermal resistance between BNNS and polymer (7.6×10^{-9} m^2 K/W)[45] and d is the average size of nanofillers.

However, the above model can be applied only to isotropic porous materials, meaning that the *k* values in the alignment and transverse directions of anisotropic aerogels cannot be separately estimated. Therefore, it is necessary to formulate a new model to predict the *k* values of anisotropic aerogels in both directions. Given the highly aligned pores, they can be estimated using a simplified parallel model originally devised for unidirectional fiber-reinforced composites[46] (Eq. (4)) for the k_{align} and a modified model based on the total thermal resistor network[47] (Supplementary Figure 3) (Eq. (5)) for the k_{trans}, assuming that all pore channels have

the same diameter and are perfectly parallel to one another. The *k* of matrix and unidirectional fibers in the composites are replaced by those of cell walls, namely k_{wall}^{x} and k_{wall}^{y} in the transverse and alignment directions, and air in pore channels (k_0^g) in aerogels, respectively. In addition, the fiber volume fraction of composites is substituted with the porosity of aerogels (φ). Therefore, the conduction components in the alignment and transverse directions, k_{align} and k_{trans}, are given:

$$k_{align} = (1 - \varphi)k_{wall}^{y} + \varphi\, k_0^g \quad (4)$$

$$k_{trans} = \frac{0.5(1+\varphi)^2 k_0^g k_{wall}^{x} + \varphi(1-\varphi)(k_{wall}^{x})^2}{\varphi(1-\varphi)k_0^g + 2\varphi k_{wall}^{x}} \quad (5)$$

The *k* of the BNNS/WPU composite cell wall in the transverse and alignment directions, *i.e.*, k_{wall}^{x} and k_{wall}^{y}, are estimated using the effective medium approximation according to previous studies (see Supplementary Information for details).[48, 49] The calculated *k* of highly anisotropic BNNS/WPU aerogels at different porosities are presented as solid lines in Figure 3d and 3e. It is shown that the effect of BNNS loading on *k* was more significant in the alignment direction than in the transverse direction. This is because the 2D structure of BNNS facilitated the in-plane heat transfer and mitigated the heat conduction transverse to it. Moreover, the lower was the porosity, φ, of composite aerogels, the higher was the *k* in both directions, which was expected due to the higher solid content. The experimental k_{align} of the composite aerogel freeze-dried at -196 ˚C having a porosity of 98% was compatible with the theoretical prediction (Figure 3d). In a sharp contrast to alignment direction, the effect of BNNS loading on k_{trans} was almost negligible with only a marginal increase with increasing filler loading. The anisotropic *k* values predicted at a porosity of 98% agreed well with experimental trends observed from this work and a previous study.[8] It is noteworthy that the predictions from the isotropic model using Eqs. (1) – (3) manifested monotonic increases in *k* with the increasing BNNS loading along both directions (blue dash lines in Figure 3d and e), unable to accurately reflect the anisotropic *k*. The experimental k_{trans} of the composite aerogel with 98% porosity

was lower than the theoretical value because the cell walls were assumed not to contain holes in the calculation. Contrary to the assumption, however, there were many holes in the cell walls as shown in Supplementary Figure 4 with an associated extremely low solid content of 1.4 wt% in the aerogel. The extra solid-air interfaces created by the holes inevitably increased the phonon heat transport path, lowering the k to below that of air.[50] In general, the proposed anisotropic model indicates that the addition of BNNS improved the anisotropic factor, R, of composite aerogels for all porosities, as shown in Figure 3f.

To summarize, a high anisotropic factor resulting from the higher k_{align} than k_{trans} effectively directed the heat flow in the pore alignment direction while reducing the transverse heat transfer, translating into better thermal insulation performance of anisotropic aerogels than their isotropic counterparts.[51] The highly anisotropic structure of BNNS/WPU composite aerogels fabricated using the lowest freezing temperature of -196 ˚C enabled the heat dissipation in the alignment direction, while their heat conduction in the transverse direction was diminished, achieving an ultralow k_{trans} of 16.2 mW/m K. Several parameters were identified to be critical to achieve a high anisotropic factor. First, a highly anisotropic structure is fundamental to a high anisotropic factor. Unidirectional freeze-casting is an effective method to construct highly anisotropic aerogels and foams with aligned pores,[52-55] constituting a good basis for attaining high anisotropic factors. Second, a low freezing temperature is essential to attain small pores and good pore alignments, beneficial to a high anisotropic factor. Third, the intrinsic anisotropic k of BNNS[56] also contributes to high anisotropic factors by aligning them in the pore walls. The theoretical calculations also proved that the use of BNNS can effectively improve the k_{align} without significantly increasing the k_{trans}, demonstrating great potential of BNNS for anisotropic thermal management applications.

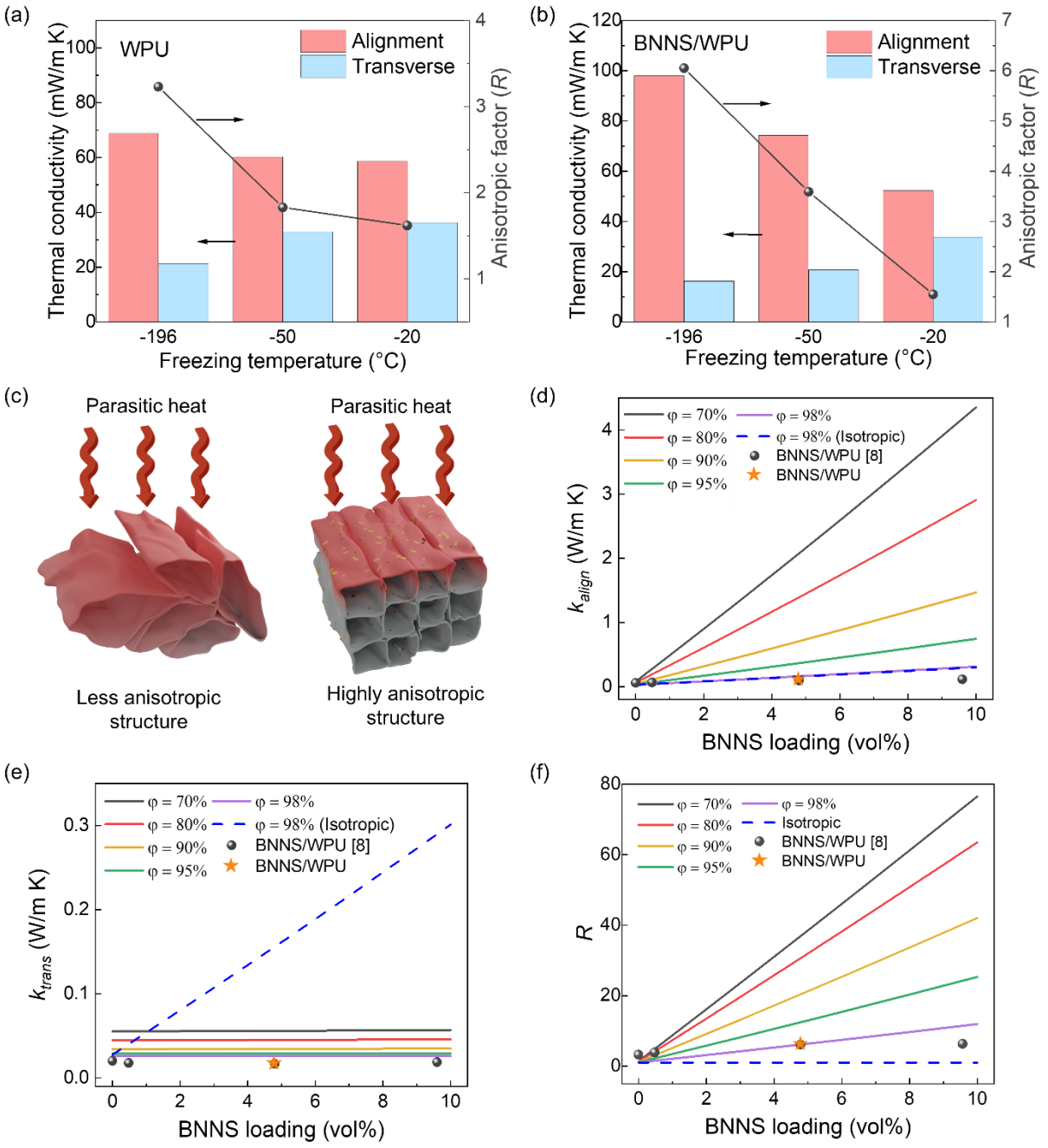

Figure 3. Thermal superinsulation performance of anisotropic BNNS/WPU aerogels. k_{align}, k_{trans} and the resultant anisotropic factor (R) of (a) WPU and (b) BNNS/WPU composite aerogels prepared at different freezing temperatures. (c) Schematic of the highly anisotropic structure responsible for ultralow k_{trans} in comparison with a less anisotropic aerogel. Effects of BNNS loading on theoretical k of anisotropic BNNS/WPU aerogels with different porosities in the (d) alignment and (e) transverse directions in comparison with experimental data and

theoretical isotropic *k* at a porosity of 98%. (f) Predicted *R* of composite aerogels with different porosities and BNNS loading.

2.3 Sunlight reflectance performance of BNNS/WPU composite aerogels

To reduce the underlying heat gain in daytime, composite aerogels were designed to provide high sunlight reflectance. Both the BNNS/WPU and WPU aerogels freeze-dried at -196 ˚C showed much better sunlight reflectance performance than the EPS foam with a commercial reflective coating over the whole solar wavelength from 0.3 to 2.5 μm, as shown in Figure 4a. The pristine WPU aerogels freeze-dried at -196 ˚C exhibited exceptionally high sunlight reflectance of ~97% which is 12% and 27% higher than those freeze-cast at higher temperatures of -50 ˚C and -20 ˚C, respectively (Figure 4b). The larger number of air/solid interfaces created by the smaller ice crystals at a lower freezing temperature was responsible for this finding. The underlying mechanisms are schematically illustrated in Figure 4c with reference to the SEM images given in Figure 2d-k. The mismatch in refractive indices of air and solid cell wall (i.e., polymer) led to strong light scattering at the air/solid interfaces, giving rise to an improved sunlight reflectance. It is of note that the enhancing effect of BNNS on sunlight reflectance was more significant when a higher freezing temperature was applied. The different enhancement effects of BNNS on solar reflectance of composite aerogels could be attributed to different scattering mechanisms arising from different pore dimensions obtained at different freezing temperatures.[57] The small pore sizes in the WPU aerogel prepared at – 196 °C gave rise to effective light scattering at the numerous solid/air interfaces and thus a high solar reflectance of 97%. Because of the predominant role of small pores, the additional ameliorating effect brought by BNNS was not clearly visible for this composite aerogel. In contrast, the WPU aerogels freeze-cast at – 50 and – 20 °C showed relatively poor reflectances of 86% and 76%, respectively, primarily because of the larger pore sizes and thus less effective scattering than their counterpart obtained at – 196 °C. Given the limited contribution of large pores, the

addition of BNNS led to significant enhancement in reflectance of the BNNS/WPU aerogels attained at these high temperatures thanks to the additional scattering occurring at the BNNS/WPU interfaces. In addition, BNNS with a higher refractive index than that of WPU increased the effective refractive index of cell walls and further magnified the mismatch of refractive indices between the cell walls and air, leading to strong light scattering at the solid/air interfaces. The mismatch of refractive indices between BNNS and polymer also contributed to extra light scattering at the BNNS/polymer interfaces, further enhancing the sunlight reflectance. To conclude, both a low freezing temperature and addition of BNNS offered facile approaches to achieve excellent sunlight reflectance. The k_{trans} and solar reflectance of the BNNS/WPU aerogel are compared with other thermally insulating and solar reflective structures reported in the literature,[4, 5, 58-63] as shown in Supplementary Table 2. The current BNNS/WPU aerogel exhibited the highest solar reflectance (97%) with one of the lowest k_{trans} (16.2 mW/m K) among different structures, although the hollow microfibers cooler[62] showed a marginally lower k_{trans} (14 mW/m K) than our BNNS/WPU aerogel. Nonetheless, the aligned pores in the BNNS/WPU aerogel simultaneously delivered a high k_{align} for heat dissipation in the in-plane direction to avoid heat localization, which was not available for the hollow microfibers cooler. The comparison signifies the excellent optical and thermal properties of the BNNS/WPU aerogel for outdoor thermal insulation applications.

To investigate the thermal insulating performance in practical applications, the BNNS/WPU aerogel freeze-dried at -196 ˚C was tested in an outdoor condition using the set-up similar to the previous study[8] (details in the Experimental section and Supplementary Figure 5). The sample served as the top surface of an enclosure and was exposed under direct sunlight. The test was carried out on a clear day (12 October 2022) in Hong Kong. The solar irradiance during the test was recorded using a solar meter, as shown in Figure 4d. The internal temperature variations within the enclosure were also monitored using a thermocouple. The BNNS/WPU aerogel outperformed, maintaining a lower internal temperature during the whole test than the

SiO_2 blanket, and EPS foam coated with commercial reflective paint (Figure 4d). This finding is congruent with the lower *k* of BNNS/WPU (16.2 mW/m K) than SiO_2 (~40 mW/m K) and EPS (30.5 mW/m K), reduced the parasitic heat gain from hot ambient. Together with the sunlight reflectance of BNNS/WPU of ~97% which can minimize the solar heat gain, the BNNS/WPU composite aerogel exhibited an up to 6 ˚C lower internal temperature than the SiO_2 blanket and EPS foam with a reflective coating during 13:00 – 14:30 of which the solar irradiance ranged 0.8 – 0.9 kW/m^2, demonstrating a better cooling effect than commercial products under direct sunlight.

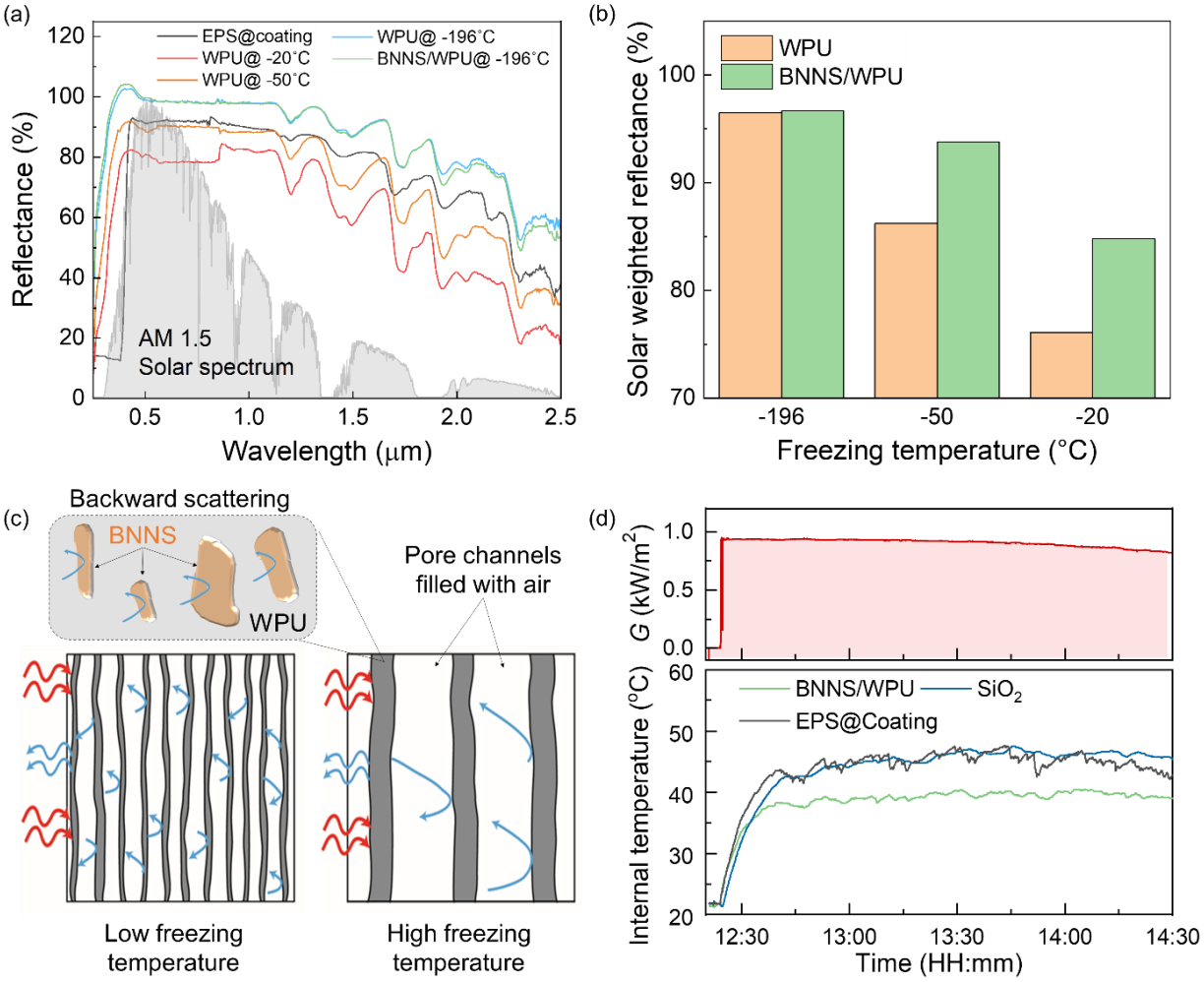

Figure 4. Solar reflectance of BNNS/WPU aerogels. (a) Ultraviolet-visible-near infrared (UV-vis-NIR) spectra of WPU aerogels fabricated at different freezing temperatures in comparison to commercial EPS foam coated with highly reflective paint. (b) Solar weighted

reflectance of WPU and BNNS/WPU aerogels. (c) Sunlight reflecting mechanisms of aerogels prepared at low and high freezing temperatures. (d) Solar irradiance (*G*) and internal temperature changes in BNNS/WPU aerogels in comparison with commercial SiO_2 blanket and EPS coated with reflective paint, measured on the campus of HKUST in Hong Kong, SAR on 12th October 2022.

3. Conclusion

The anisotropic factor (*R*) of WPU aerogels was successfully tailored by controlling the freezing temperature used in the unidirectional freeze-casting process and incorporating 2D BNNS in WPU. WPU aerogels freeze-dried at -196 °C exhibited the highest *R* of 3.2 due to the highly anisotropic and intact structures created at a low freezing temperature of -196 ˚C. The *R* of WPU aerogel was further increased to 6.0 by adding BNNS into cell walls, fully exploiting the anisotropic *k* of BNNS and therefore achieving an ultralow k_{trans} of 16.2 mW/m K, even lower than k_{air}. A new theoretical model was proposed to estimate the anisotropic *k* of porous materials, confirming the positive effect of BNNS addition on improving the *R* of aerogel. The abundant solid/air interfaces provided by the highly porous structure promoted extensive light scattering and thus ameliorated the sunlight reflectance of WPU aerogels. The addition of BNNS further enhanced the solar reflectance to a maximum of ~97% by magnifying the refractive index mismatch between air and solid cell walls and facilitating extra light scattering between BNNS and polymer. Combining the synergy arising from the superinsulation performance and exceptional solar reflectance, the BNNS/WPU composite aerogel exhibited an up to 6 °C lower internal temperature than commercial products in the outdoor test, promising great potential for highly energy-efficient cooling in building applications.

4. Experimental Section

4.1. Fabrication of BNNS/WPU aerogel

The fabrication of WPU aerogels at different freezing temperature was schematically described in Figure 1a. The BNNS/WPU aerogels were fabricated by dispersing BNNS in WPU, followed by unidirectional freezing at three different temperatures: -20, -50 and - 196 ˚C. The pristine 1.4 wt% WPU solution was prepared by diluting WPU (NeoRez R610 supplied by DSM, NeoResin) with DI water. 10wt% BNNS was dispersed in the WPU solution by magnetic stirring for 48 h to obtain the BNNS/WPU dispersion. The dispersion was poured into a mold consisting of thermally insulating Styrofoam sides and a thermally conductive aluminum bottom for unidirectional freeze casting along the vertical direction.[64] The freezing temperature was controlled by metal plate in contact with different cold sources, including liquid nitrogen (-196 ˚C) and freezers at -20 and -50 ˚C. The different temperature gradients along the vertical direction formed anisotropic structures with differing ice crystal sizes. The frozen samples were freeze-dried for 120 h to obtain BNNS/WPU aerogels. The porosity of aerogel was calculated from Eq. (6):[8]

$$Porosity = \left(1 - \frac{\rho}{\rho_0}\right) \times 100\% \quad (6)$$

where ρ is the apparent density of the aerogel and ρ_0 is the density of the corresponding solid composite estimated from the volume-averaged densities of WPU (1.02 g/cm^3) and BNNS (2.25 g/cm^3). The porosities calculated for different aerogels are shown in Supplementary Table 1.

4.2. Characterizations of BNNS/WPU aerogel

SEM (TM3030) was used to characterize the morphologies of BNNS/WPU aerogels freeze-dried at different temperatures. The crystal structures of the bulk *h*-BN and BNNS were confirmed by X-ray diffraction with a CuKα radiation source from 20º to 60º (XRD, PW1830, Philips). FTIR spectroscopy, Bruker Vertex 70) was used to examine the chemical compositions of BNNS, WPU and BNNS/WPU. The atomic force microscopy (AFM, Scanning Probe Microscope-Dimension ICON) was used to characterize the thickness profile of BNNS.

The thermal conductivities of BNNS/WPU aerogels were measured on a Hot Disk Thermal Constants Analyzer (TPS 2500S). The thermal insulation property of BNNS/WPU aerogels was demonstrated using an infrared (IR) camera (Fluke Ti25). The samples were placed on a hot plate at 85 ºC and the temperatures of the BNNS/WPU aerogel and commercial EPS foam were measured using the IR camera. UV-vis-NIR spectroscopy (Perkin Elmer Lambda 950) was used to measure the sunlight reflectance performance of the WPU and composite aerogels. The reflectance spectrum was converted to weighted solar reflectance according to ASTM G173.

The outdoor tests were conducted using an EPS foam box with the testing sample covering the top to form an enclosure (Supplementary Figure 5). The enclosure had inner dimensions of 35 mm (length) × 35 mm (width) × 20 mm (height). All samples including commercial EPS foam, SiO_2 blanket, and BNNS/WPU aerogel were in the same dimensions of 40 mm (length) × 40 mm (width) × 9 mm (thickness), ensuring full coverage of the top surface of the enclosures. The sample was directly exposed to the sunlight while all other faces of the EPS foam box were covered by aluminum foils to diminish the solar heat absorption. A polyethylene film was placed beneath the test samples to minimize the convection between the interior and ambient environment.[8, 65] The solar irradiance and temperature were monitored using a solar meter (TES-1333R Solar Power Meter) and a thermocouple (CENTER-309 Portable Digital Thermometer), respectively.

Acknowledgement

This project was supported by the Research Grants Council (GRF Projects: 16205517 and 16200720) and the Innovation and Technology Commission (ITS/012/19) of Hong Kong SAR, and start-up fund for new recruits of PolyU (P0038855 and P0038858). This project was also supported by the Research Institute for Sports Science and Technology of PolyU (P0043535). Technical assistance from the Materials Characterization and Preparation

Facilities (MCPF) and the Advanced Engineering Material Facility (AEMF) of HKUST are appreciated.

Conflict of interest

The authors declare no conflict of interest.

References

1. T. Qian, J. Li, X. Min, W. Guan, Y. Deng and L. Ning, *J. Mater. Chem. A*, 2015, **3**, 8526-8536.
2. Z. Qian, Z. Wang, Y. Chen, S. Tong, M. Ge, N. Zhao and J. Xu, *J. Mater. Chem. A*, 2018, **6**, 828-832.
3. G. Hayase, K. Kugimiya, M. Ogawa, Y. Kodera, K. Kanamori and K. Nakanishi, *J. Mater. Chem. A*, 2014, **2**, 6525-6531.
4. J. Yang, K.-Y. Chan, H. Venkatesan, E. Kim, M. H. Adegun, J.-H. Lee, X. Shen and J. K. Kim, *Nano-Micro Lett.*, 2022, **14**, 54.
5. Z.-L. Yu, N. Yang, L.-C. Zhou, Z.-Y. Ma, Y.-B. Zhu, Y.-Y. Lu, B. Qin, W.-Y. Xing, T. Ma and S.-C. Li, *Sci. Adv.*, 2018, **4**, eaat7223.
6. X. Zhang, X. Zhao, T. Xue, F. Yang, W. Fan and T. Liu, *Chem. Eng. J.*, 2020, **385**, 123963.
7. B. Wicklein, A. Kocjan, G. Salazar-Alvarez, F. Carosio, G. Camino, M. Antonietti and L. Bergström, *Nat. Nanotechnol.*, 2015, **10**, 277-283.
8. K.-Y. Chan, X. Shen, J. Yang, K.-T. Lin, H. Venkatesan, E. Kim, H. Zhang, J.-H. Lee, J. Yu and J. Yang, *Nat. Commun.*, 2022, **13**, 1-12.
9. W. Xiao, P. Wang, X. Song, B. Liao, K. Yan and J.-J. Zhang, *ACS Sustain. Chem. Eng.*, 2021, **9**, 9348-9357.
10. S. E. Kim, F. Mujid, A. Rai, F. Eriksson, J. Suh, P. Poddar, A. Ray, C. Park, E. Fransson and Y. Zhong, *Nature*, 2021, **597**, 660-665.
11. A. A. Balandin, *Nat. Mater.*, 2011, **10**, 569-581.
12. P. Jiang, X. Qian, R. Yang and L. Lindsay, *Phys. Rev. Mater.*, 2018, **2**, 064005.
13. S. Yu, X. Shen and J.-K. Kim, *Mater. Horiz.*, 2021, **8**, 3009-3042.
14. X. Shen, Q. Zheng and J.-K. Kim, *Prog. Mater. Sci.*, 2021, **115**, 100708.
15. K. Watanabe, T. Taniguchi and H. Kanda, *Nat. Mater.*, 2004, **3**, 404-409.
16. Z. Yang, Z. Zhou, H. Sun, T. Chen and J. Zhang, *Compos. Sci. Technol.*, 2021, **207**, 108743.
17. D. Miao, X. Wang, J. Yu and B. Ding, *Adv. Funct. Mater.*, 2021, **31**, 2008705.
18. J. Chen, X. Huang, B. Sun and P. Jiang, *ACS Nano*, 2018, **13**, 337-345.
19. X. Xu, Q. Zhang, M. Hao, Y. Hu, Z. Lin, L. Peng, T. Wang, X. Ren, C. Wang and Z. Zhao, *Science*, 2019, **363**, 723-727.

20. B. Wang, G. Li, L. Xu, J. Liao and X. Zhang, *ACS Nano*, 2020, **14**, 16590-16599.
21. J. Yang, X. Shen, W. Yang and J.-K. Kim, *Prog. Mater. Sci.*, 2022, 101054.
22. X. Shen and J.-K. Kim, *Nano Res.*, 2022, 1-27.
23. S. Deville, E. Saiz, R. K. Nalla and A. P. Tomsia, *Science*, 2006, **311**, 515-518.
24. J. Yang, W. Yang, W. Chen and X. Tao, *Prog. Polym. Sci.*, 2020, **109**, 101289.
25. S. Deville, *Freezing colloids: observations, principles, control, and use: applications in materials science, life science, earth science, food science, and engineering*, Springer, 2017.
26. J. Li, T. Ye, B. Zhou and B. Li, *RSC Adv.*, 2014, **4**, 22251-22254.
27. L. L. Reys, S. S. Silva, R. P. Pirraco, A. P. Marques, J. F. Mano, T. H. Silva and R. L. Reis, *Eur. Polym. J.*, 2017, **95**, 232-240.
28. X. Xu, Q. Zhang, Y. Yu, W. Chen, H. Hu and H. Li, *Adv. Mater.*, 2016, **28**, 9223-9230.
29. Z. Guo, Y. Li, P. Jin, T. Zhang, Y. Zhao, Y. Ai, H. Xiu, Q. Zhang and Q. Fu, *Polymer*, 2021, **230**, 124101.
30. Z. Yu, T. Dai, S. Yuan, H. Zou and P. Liu, *ACS Appl. Mater. Interfaces*, 2020, **12**, 30990-31001.
31. Z. Zeng, X. Y. D. Ma, Y. Zhang, Z. Wang, B. F. Ng, M. P. Wan and X. Lu, *ACS Sustain. Chem. Eng.*, 2019, **7**, 6959-6968.
32. Y. Gu, X. Mu, P. Wang, X. Wang, J. Liu, J. Shi, A. Wei, Y. Tian, G. Zhu, H. Xu, J. Zhou and L. Miao, *Nano Energy*, 2020, **74**, 104857.
33. Y. Tian, D. Estevez, H. Wei, M. Peng, L. Zhou, P. Xu, C. Wu, M. Yan, H. Wang and H.-X. Peng, *Chem. Eng. J.*, 2021, **421**, 129781.
34. S. M. Jung, D. L. Mafra, C.-T. Lin, H. Y. Jung and J. Kong, *Nanoscale*, 2015, **7**, 4386-4393.
35. X. Zhu, C. Yang, P. Wu, Z. Ma, Y. Shang, G. Bai, X. Liu, G. Chang, N. Li and J. Dai, *Nanoscale*, 2020, **12**, 4882-4894.
36. D. Lee, B. Lee, K. H. Park, H. J. Ryu, S. Jeon and S. H. Hong, *Nano Lett.*, 2015, **15**, 1238-1244.
37. E. Kim, H. Zhang, J.-H. Lee, H. Chen, H. Zhang, M. H. Javed, X. Shen and J.-K. Kim, *Compos. Part A Appl. Sci. Manuf.*, 2021, **147**, 106430.
38. X. Li, P. Bandyopadhyay, T. Kshetri, N. H. Kim and J. H. Lee, *J. Mater. Chem. A*, 2018, **6**, 21501-21515.
39. Z. Gao, C. Zhi, Y. Bando, D. Golberg and T. Serizawa, *ACS Appl. Mater. Interfaces*, 2011, **3**, 627-632.
40. X. Shen and J.-K. Kim, *Funct. Compos. Mater.*, 2020, **2**, 022001.
41. V. Apostolopoulou‐Kalkavoura, P. Munier and L. Bergström, *Adv. Mater.*, 2021, **33**, 2001839.
42. M. J. Oh, J. H. Lee and P. J. Yoo, *Adv. Funct. Mater.*, 2021, **31**, 2007392.
43. J. Guo and G. Tang, *Int. J. Heat Mass Transf.*, 2019, **137**, 64-73.
44. P. Collishaw and J. Evans, *J. Mater. Sci.*, 1994, **29**, 2261-2273.
45. Z.-G. Wang, W. Liu, Y.-H. Liu, Y. Ren, Y.-P. Li, L. Zhou, J.-Z. Xu, J. Lei and Z.-M. Li, *Compos. B Eng.*, 2020, **180**, 107569.

46. R. Singh and H. Kasana, *Appl. Therm. Eng.*, 2004, **24**, 1841-1849.
47. L.-W. Fan, Y.-C. Hu, T. Tian and Z.-T. Yu, *Int. J. Heat Mass Transf.*, 2006, **49**, 4116-4123.
48. C.-W. Nan, R. Birringer, D. R. Clarke and H. Gleiter, *J. Appl. Phys.*, 1997, **81**, 6692-6699.
49. X. Shen, Z. Wang, Y. Wu, X. Liu, Y.-B. He and J.-K. Kim, *Nano Lett.*, 2016, **16**, 3585-3593.
50. A. Rizvi, R. K. Chu and C. B. Park, *ACS Appl. Mater. Interfaces*, 2018, **10**, 38410-38417.
51. H. Zhang, X. Shen, E. Kim, M. Wang, J. H. Lee, H. Chen, G. Zhang and J. K. Kim, *Adv. Funct. Mater.*, 2022, **32**, 2111794.
52. P. Liu, X. Li, P. Min, X. Chang, C. Shu, Y. Ding and Z.-Z. Yu, *Nano-Micro Lett.*, 2021, **13**, 1-15.
53. C. Shu, H.-Y. Zhao, S. Zhao, W. Deng, P. Min, X.-H. Lu, X. Li and Z.-Z. Yu, *Compos. B. Eng.*, 2023, **248**, 110367.
54. P. Min, J. Liu, X. Li, F. An, P. Liu, Y. Shen, N. Koratkar and Z. Z. Yu, *Adv. Funct. Mater.*, 2018, **28**, 1805365.
55. T. Liu, M. Huang, X. Li, C. Wang, C.-X. Gui and Z.-Z. Yu, *Carbon*, 2016, **100**, 456-464.
56. F. Guo, X. Shen, J. Zhou, D. Liu, Q. Zheng, J. Yang, B. Jia, A. K. Lau and J. K. Kim, *Adv. Funct. Mater.*, 2020, **30**, 1910826.
57. X.-H. Li, P. Liu, X. Li, F. An, P. Min, K.-N. Liao and Z.-Z. Yu, *Carbon*, 2018, **140**, 624-633.
58. A. Leroy, B. Bhatia, C. C. Kelsall, A. Castillejo-Cuberos, M. Di Capua H, L. Zhao, L. Zhang, A. Guzman and E. Wang, *Sci. Adv.*, 2019, **5**, eaat9480.
59. M. Yang, W. Zou, J. Guo, Z. Qian, H. Luo, S. Yang, N. Zhao, L. Pattelli, J. Xu and D. S. Wiersma, *ACS Appl. Mater. Interfaces*, 2020, **12**, 25286-25293.
60. X. Yue, H. Wu, T. Zhang, D. Yang and F. Qiu, *Energy*, 2022, **245**, 123287.
61. C. Cai, Z. Wei, C. Ding, B. Sun, W. Chen, C. Gerhard, E. Nimerovsky, Y. Fu and K. Zhang, *Nano Lett.*, 2022, **22**, 4106-4114.
62. H. Zhong, Y. Li, P. Zhang, S. Gao, B. Liu, Y. Wang, T. Meng, Y. Zhou, H. Hou and C. Xue, *ACS Nano*, 2021, **15**, 10076-10083.
63. L. An, D. Petit, M. Di Luigi, A. Sheng, Y. Huang, Y. Hu, Z. Li and S. Ren, *ACS Appl. Nano Mater.*, 2021, **4**, 6357-6363.
64. Z. Wang, X. Shen, N. M. Han, X. Liu, Y. Wu, W. Ye and J.-K. Kim, *Chem. Mater.*, 2016, **28**, 6731-6741.
65. D. Li, X. Liu, W. Li, Z. Lin, B. Zhu, Z. Li, J. Li, B. Li, S. Fan and J. Xie, *Nat. Nanotechnol.*, 2021, **16**, 153-158.